

Effect of side group on mechanically induced conductance switching in 4,4'-dipyridyl-based single-molecule junctions

Zhen Wan(万振), Chang-Feng Zheng(郑长风), Lin Liu(刘琳), Yun-Long Ge(葛云龙), Guang-Ping Zhang(张广平), Shuai Qiu(邱帅), Hui Wang(王辉), and Zong-Liang Li(李宗良)

Citation: Chin. Phys. B, 2025, 34 (**8**): 087202. DOI: 10.1088/1674-1056/adce98
http://cpb.iphy.ac.cn; http://iopscience.iop.org/cpb

What follows is a list of articles you may be interested in

Anisotropic spin transport and photoresponse characteristics detected by tip movement in magnetic single-molecule junction

Deng-Hui Chen(陈登辉), Zhi Yang(羊志), Xin-Yu Fu(付新宇), Shen-Ao Qin(秦申奥), Yan Yan(严岩), Chuan-Kui Wang(王传奎), Zong-Liang Li(李宗良), and Shuai Qiu(邱帅)

Chin. Phys. B, 2024, 33 (**4**): 047201. DOI: 10.1088/1674-1056/ad1e65

Current spin polarization of a platform molecule with compression effect

Zhi Yang(羊志), Feng Sun(孙峰), Deng-Hui Chen(陈登辉), Zi-Qun Wang(王子群), Chuan-Kui Wang(王传奎), Zong-Liang Li(李宗良), and Shuai Qiu(邱帅)

Chin. Phys. B, 2022, 31 (**7**): 077202. DOI: 10.1088/1674-1056/ac4f53

Fang-Howard wave function modelling of electron mobility in AlInGaN/AlN/InGaN/GaN double heterostructures

Yao Li(李姚) and Hong-Bin Pu(蒲红斌)

Chin. Phys. B, 2021, 30 (**9**): 097201. DOI: 10.1088/1674-1056/abea87

Theoretical design of single-molecule NOR and XNOR logic gates by using transition metal dibenzotetraaza[14]annulenes

Zi-Qun Wang(王子群), Fei Tang(唐菲), Mi-Mi Dong(董密密), Ming-Lang Wang(王明郎), Gui-Chao Hu(胡贵超), Jian-Cai Leng(冷建材), Chuan-Kui Wang(王传奎), Guang-Ping Zhang(张广平)

Chin. Phys. B, 2020, 29 (**6**): 067202. DOI: 10.1088/1674-1056/ab84cf

Unified semiclassical approach to electronic transport from diffusive to ballistic regimes

Hao Geng(耿浩), Wei-Yin Deng(邓伟胤), Yue-Jiao Ren(任月皎), Li Sheng(盛利), Ding-Yu Xing(邢定钰)

Chin. Phys. B, 2016, 25 (**9**): 097201. DOI: 10.1088/1674-1056/25/9/097201

Effect of side group on mechanically induced conductance switching in 4,4′-dipyridyl-based single-molecule junctions

Zhen Wan(万振)[1,†], Chang-Feng Zheng(郑长风)[1,†], Lin Liu(刘琳)[1], Yun-Long Ge(葛云龙)[1], Guang-Ping Zhang(张广平)[1,‡], Shuai Qiu(邱帅)[1], Hui Wang(王辉)[2], and Zong-Liang Li(李宗良)[1,§]

[1] *Shandong Key Laboratory of Medical Physics and Image Processing & Shandong Provincial Engineering and Technical Center of Light Manipulations, School of Physics and Electronics, Shandong Normal University, Jinan* 250358, *China*

[2] *College of Physics and Electronic Engineering, Qilu Normal University, Jinan* 250200, *China*

(Received 11 February 2025; revised manuscript received 11 March 2025; accepted manuscript online 21 April 2025)

The forming processes of 4,4′-dipyridyl-based single-molecule junctions and mechanically induced conductance switching as well as the side-group effects are systematically investigated by applying the *ab initio*-based adiabatic geometric optimization method and the one-dimensional transmission combined with three-dimensional correction approximation (OTCTCA) method. The numerical results show that for the 4,4′-dipyridyl with a π-conjugated phenyl-phosphoryl or diphenylsilyl side group, the pyridyl vertically anchors on the second atomic layer of the pyramid-shaped Au tip electrode at small inter-electrode distances by laterally pushing the apical Au atom aside, which induces stronger pyridyl-electrode coupling and high-conductance state of the formed junctions. As the inter-electrode distance increases, the pyridyl shifts to the apical Au atom of the tip electrode. This apical Au atom introduces additional scatterings to the tunneling electrons and significantly decreases the conductance of the junctions. Furthermore, for the 4,4′-dipyridyl with a phenyl-phosphoryl side group, the probability of manifesting the high-conductance state is decreased due to the oxygen atom reducing the probability of the pyridyl adsorbing on the second layer of Au tip electrode. In contrast, for the 4,4′-dipyridyl with a non-conjugated cyclohexyl-phosphoryl side group, the steric hindrance from the bulky cyclohexyl group leads the molecule to preferentially form the O–Au contact, which prevents both the high conductance and mechanically induced conductance switching of the junction. Our results provide a theoretical understanding of the side-group effects on electronic transport properties of single-molecule junctions, offering an alternative explanation for the experimental observations.

Keywords: single-molecule junction, electron transport properties, conductance switching, side-group effects

PACS: 85.65.+h, 73.63.–b, 73.63.Rt, 82.20.Wt

DOI: 10.1088/1674-1056/adce98 **CSTR:** 32038.14.CPB.adce98

1. Introduction

The miniaturization of electronic components is imperative for enhancing the performance and energy efficiency of circuits. However, this progress has encountered a bottleneck in traditional silicon-based electronics.[1,2] As a result, the use of single molecules to construct functional electronic components has emerged as one of the most promising solutions to address this challenge.[3–16] It has been found that single-molecule junctions can exhibit intriguing functionalities, such as rectification,[17–21] switching,[8,9,13,15,22–26] sensing,[27–29] logic gates.[16,30–33]

Among these various functional molecular junctions, dipyridyl-based molecular junctions (DPMJs) stand out as one of the most intriguing types due to their distinct high-low conductance switching (HLCS) behaviors.[34–45] The HLCS behaviors can be well controlled and repeated by elaborately adjusting the inter-electrode distance. Especially, the HLCS behavior of 4,4′-dipyridyl with gold electrodes has been extensively discussed.[36,37,44] Quek *et al.*[36] attributed this behavior to changes in the spatial orientation of N–Au bond relative to the 4,4′-dipyridyl backbone, which is closely influenced by variations in the tilting angle of the molecular backbone with respect to the electrode–electrode axis. These changes affect the electronic coupling between the conducting molecular orbital and electrodes. In contrast, Li *et al.*[37,44] proposed that the HLCS behavior arises from the shifting of the anchoring pyridyl on the Au tip electrode between different Au binding sites that with distinct coordination modes. Additionally, Ismael *et al.*[46] further experimentally demonstrated that the HLCS behavior of DPMJs could be inhibited or reinstated by selecting non-conjugated or conjugated side groups for the 4,4′-dipyridyl. Specifically, they observed that the HLCS behavior was suppressed when a non-conjugated cyclohexyl-phosphoryl or trimethyl-phosphoryl side group was used, but was reinstated when these were replaced with π-conjugated side groups like phenyl-phosphoryl or diphenylsilyl. They attributed this side-group effect on HLCS behavior to steric hindrance from the bulky non-conjugated groups, which re-

[†]These authors contributed equally to this work.

[‡]Corresponding author. E-mail: zhangguangping@sdnu.edu.cn

[§]Corresponding author. E-mail: lizongliang@sdnu.edu.cn

© 2025 Chinese Physical Society and IOP Publishing Ltd. All rights, including for text and data mining, AI training, and similar technologies, are reserved.

duces molecule–electrode coupling and further inhibits the high-conductance geometries. On the contrary, interactions between π-conjugated side groups and the electrode tip help restore the HLCS behavior. In their computational models, three typical contact configurations were considered, each exhibiting different conductance values. However, it remains unclear how these contact configurations transition between each other during the stretching and compressing processes of the junctions. Additionally, given the complexity and diversity of molecule–electrode contact configurations that arise during the formation of DPMJs, other plausible mechanisms for the HLCS behaviors of the 4,4′-dipyridyl derivatives may also be involved.

To address these two questions, we employed the *ab initio*-based adiabatic geometric optimization method to investigate the evolution of contact configurations and electronic transport properties of the DPMJs during the stretching and compressing processes. Our calculations demonstrate that the high-conductance state of DPMJs with the π-conjugated side groups arises from strong molecule–electrode coupling and a large electronic incident cross-section area in the contact configuration where one pyridyl anchors to the apical Au atom on one electrode while the other pyridyl nearly vertically anchors to the second atomic layer of the Au tip electrode when the inter-electrode distance is small. Compared to the junction with the diphenylsilyl side group, the likelihood of exhibiting the high-conductance state for the junction with the phenyl-phosphoryl is reduced because the oxygen atom lowering the probability of the pyridyl adsorbing on the second layer of Au tip electrode. In contrast, due to significant steric hindrance from the bulky cyclohexyl-phosphoryl side group, the junction with the phosphoryl group preferentially connects to the Au tip electrode via the oxygen atom, preventing the pyridyl from adsorbing onto the second Au atomic layer and inhibiting the high-conductance state.

2. Theoretical model and computational details

The schematic structures of the DPMJs with different side groups are shown in Fig. 1. M1 comprises a 4,4′-dipyridyl with a diphenylsilyl side group, M2 consists of a 4,4′-dipyridyl with a phenyl-phosphoryl, and M3 contains a 4,4′-dipyridyl with a cyclohexyl-phosphoryl side group. Considering the fact that these molecular junctions were experimentally investigated with the scanning tunneling microscopy-break junction (STM-BJ) technique, during the stretching process, the pyramid Au cluster or an isolated Au atom is most likely formed on the surface of the bottom electrode once the electrode–electrode contact breaks. To simulate this, we use a pyramid-shaped electrode to represent the gold tip electrode and a planar Au (111) electrode with an isolated Au adatom on the surface to model the bottom electrode.

Considering the fact that in the experiment the speed of stretching or compressing the electrodes is much slower than the thermal velocities for atoms in the molecule and at the electrode surfaces, then the configuration evolution of the DPMJs during the stretching and compressing processes can be theoretically studied using the *ab initio*-based adiabatic geometric optimization method. In this method, the inter-electrode distance D is adjusted by a step of 0.2 Å to simulate the stretching and compressing processes of STM-BJs. For each inter-electrode distance step, the optimized geometry for the last step is used as the initial geometry for the current step. Test calculations suggest that only the Au atoms in the proximity of the 4,4′-dipyridyl derivative have visible variations in coordinates during the geometric optimizations. Therefore, the 4,4′-dipyridyl derivative and four nearest Au atoms in each electrode are fully relaxed while the rest Au atoms in the electrode are fixed at their bulk coordinate positions to sustain the stretching or compressing force from the bulk electrodes. By this, the single-point energy E of the single-molecule junctions with different electrode distance D can be obtained. Then, the stretching and compressing force F is evaluated according to $F = \partial E/\partial D \approx \Delta E/\Delta D$. This approach has been proved reliable and efficient.[37,44,47–49] The *ab initio* simulations are performed within the Gaussian16 package[50] with B3LYP functional and the Lanl2DZ basis set. In the geometric structure optimizations, the convergence criterion is 0.023 eV/Å for the maximum force on each relaxed atom and 0.0015 eV/Å for the root mean square (RMS) of all relaxed atomic forces. Meanwhile, the convergence criterion for self-consistent field (SCF) procedure is set to 10^{-6} for the RMS change and 10^{-4} for the maximum change in the density matrix.

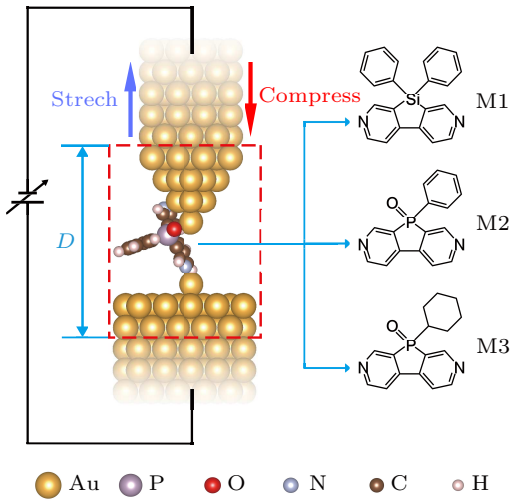


Fig. 1. The schematic structures of the DPMJs. The structures in the dashed rectangular box are the systems on which we performed configuration evolution simulations. M1, M2, and M3 are 4,4′-dipyridyl with diphenylsilyl, phenyl-phosphoryl, and cyclohexyl-phosphoryl side groups, respectively.

Since the conductance is measured under a low bias voltage V (typically $V \leq 0.3$ V) in the experiment, the electronic

transport in the molecular junctions is in the non-resonant regime. To calculate the non-resonant electronic transmission spectrum, we use our home-developed one-dimensional (1D) transmission combined with three-dimensional (3D) correction approximation (OTCTCA) method, which not only can provide conductance values consistent with experimental observations in magnitude but also can offer an intuitive physical picture to elucidate the differences between the high- and low-conductance states of the molecular junctions.[51] Within this approach, the conductance is expressed as

$$G = \frac{eS}{V}\int j_z(E)[f_S(E)\rho_S(E) - f_D(E)\rho_D(E)]T(E)\mathrm{d}E, \quad (1)$$

where e is the electronic charge, S is the incident area of electrons from electrodes, j_z is the electron probability flux density along the transport z direction within the incident area S.[52] $f_S(E)$ and $f_D(E)$ are the Fermi–Dirac distributions of electrons in the source and drain electrodes, respectively. $\rho_S(E)$ and $\rho_D(E)$ are the densities of states (DOS) of the source and drain electrodes, respectively. $T(E)$ is the statistically averaged electronic transmission probability over a large number of individual transmission probabilities, $\tau_i(E)$, for the i transport channel within the incident area S, according to $T(E) = (1/N)\sum_{i=1}^{N}\tau_i(E)$. The number of transport channels N is proportional to the chosen incident area S. Therefore, the product of S and $T(E)$ at a specific energy E converges quickly as S increases. The individual transmission probability $\tau_i(E)$ is highly depends on the profile and path length of the spatial potential field along the transport channel in the scattering region and can be approximately calculated by solving the 1D Schrödinger equation combined with 3D corrections. Refer to Ref. [51] for more calculation details of the above quantities.

3. Results and discussion

3.1. Evolution of molecule–electrode contact configurations for investigated DPMJs with different side groups

Figure 2 illustrates the configuration evolution of the investigated DPMJs during the stretching and compressing processes. Generally, when the inter-electrode distance is small after the Au–Au contact breaks, the 4,4′-dipyridyl backbone trends to anchor to the Au adatom on the substrate electrode through N–Au binding, while the upper part of the molecule adsorbs onto the side of the upper electrode tip via the other pyridyl group (as shown in Fig. 1). As the inter-electrode distance increases, different configuration evolutions occur for these DPMJs with various side groups. For M1, when the inter-electrode distance is stretched to 2.02 nm, the upper pyridyl almost vertically adsorbs onto the second Au atomic layer by the N atom, while the top Au atom is pushed aside. This configuration is referred to as the S-type configuration for brevity. When the inter-electrode distance is stretched to 2.23 nm, the upper pyridyl abruptly shifts from the second Au atomic layer to the apical Au atom of the upper tip electrode, with the apical Au atom returning to its original lattice position. This configuration is denote as the T-type configuration. As the inter-electrode distance is stretched to 2.48 nm, the M1 junction is broken. In contrast, when the tip electrode is compressed towards the substrate electrode from a large inter-electrode distance, the M1 junction is reconstructed at 2.46 nm, with the N atom adsorbing onto the apical Au atom of the upper tip electrode. As the tip electrode is further compressed, the M1 backbone bends until the upper pyridyl shifts to the second Au atomic layer of the upper tip electrode at an inter-electrode distance of 2.13 nm.

For the M2 junction, two possible configuration evolutions can occur due to the phenyl-phosphoryl side group containing an oxygen atom. In the first configuration, when the molecule initially migrates into the electrode gap, the oxygen atom of the phenyl-phosphoryl side group points outward. The nitrogen atom in the upper pyridyl group first binds to the second atomic Au layer of the upper tip electrode, forming the S-type configuration at an inter-electrode distance of 2.02 nm. As the inter-electrode distance is increased to 2.22 nm, the apical Au atom of the tip electrode returns to its initial lattice position, and the upper pyridyl shifts to bind to the apical Au atom, forming the T-type configuration. The M2 junction breaks when the inter-electrode distance is stretched to 2.48 nm. During the compressing process, the M2 junction is rebuilt at 2.46 nm, with the pyridyl group first anchoring onto the apical Au atom of the upper tip electrode. As the inter-electrode distance is further reduced to 2.11 nm, the upper pyridyl of M2 shifts to bind to the second Au atomic layer of the upper tip electrode. In the second configuration, the oxygen atom migrates into the electrode gap when the junction is formed. Initially, the oxygen atom adsorbs onto the apical Au atom of the upper tip electrode (denoted as O-type configuration), which significantly hinders the upper pyridyl from binding to the second Au atomic layer of the upper electrode tip. The oxygen atom detaches from the upper electrode tip until the inter-electrode distance is stretched to 2.32 nm. At this time, the nitrogen atom of the upper pyridyl naturally anchors onto the apical Au atom of the upper electrode tip. During the compressing process for the second configuration, as the inter-electrode distance decreases, the backbone of the M2 molecule gradually bends until the oxygen atom rebinds to the apical Au atom at 2.15 nm.

The configuration evolution of the M3 junction shares similarities with that of the M2 junction to some extent. There are also two possible configuration evolution for the M3 junction. If the the oxygen atom of the cyclohexyl-phosphoryl side

group points outward when the molecule initially migrates into the electrode gap, the upper pyridyl tends to anchor onto the second Au atomic layer of the upper tip electrode, forming the S-type configuration at an inter-electrode distance of 2.01 nm while pushing the apical Au atom aside. As the distance increases to 2.21 nm, the upper pyridyl shifts to connect with the apical Au atom by pulling the apical Au atom back to its original lattice position to form the T-type configuration. However, when compressing the M3 molecular junction from the T-type configuration to an inter-electrode distance of 2.19 nm, the oxygen atom always preferentially bonds to the apical Au atom to form the O-type configuration, which hinders the nitrogen atom of the upper pyridyl from anchoring onto the second Au atomic layer of the upper tip electrode. As a result, for the M3 molecular junction, the S-type configuration cannot be maintained during the stretching and compression process. It is differs significantly from the case of the M2 junction, highlighting the distinct influence of the conjugated side groups *versus* the non-conjugated side group on the configuration evolution. This can be attributed to that the bulky cyclohexyl-phosphoryl side group of the M3 junction has a significant steric effect while the phenyl-phosphoryl side group of the M2 junction has attractive interaction with the tip electrode. In contrast, for the second configuration evolution, the M3 junction follows a nearly identical evolution to that of the M2 junction. That is, if the O-type configuration is initially formed for the M3 junction, the oxygen atom, rather than the upper pyridyl, adsorbs onto the apical Au atom of the upper tip electrode. The oxygen atom detaches from the apical Au atom until the inter-electrode distance is stretch to 2.34 nm. Meanwhile, the upper pyridyl instead binds to the apical Au atom of the upper tip electrode. During compression, the upper pyridyl moves away from the apical Au atom of the upper tip electrode at an inter-electrode distance of 2.19 nm, and the oxygen atom subsequently rebinds to the apical Au atom of the upper tip electrode at an inter-electrode distance of 2.18 nm.

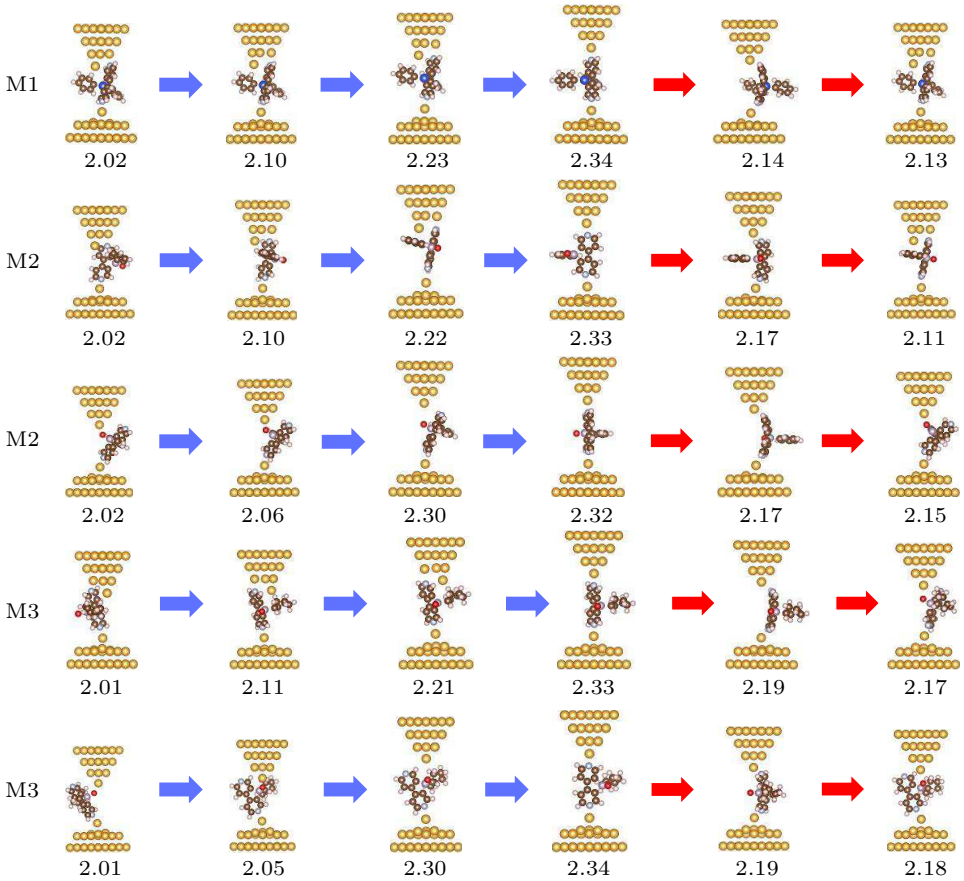


Fig. 2. Evolutions of contact configurations for the M1, M2, and M3 molecular junctions in the adiabatic stretching and compressing processes. The blue and red arrows denote the stretching and compressing processes, respectively.

It should be noted that for all three junctions, the trajectories of contact configurations are not fully reversible for the stretching and compressing processes. This feature can also be seen in the evolution of energy, force, and conductance with respect to the inter-electrode distance.

3.2. Energy and force of the investigated DPMJs with different side groups

Figure 3 shows the variations in energy of the three DPMJs during the adiabatic stretching and compressing processes and the derived force exerted on the junctions by the bulk

electrodes. It is evident that for all three junctions, there are ranges of inter-electrode distances (shaded in pale yellow-green) where the evolution of the energy and forces is not fully reversible for the stretching and compressing processes. These correspond to the irreversible evolution of the contact configurations for the stretching and compressing processes shown in Fig. 2. The energy minima for the S-type configuration of all the three junctions arise at an inter-electrode distance of 2.11 nm. In contrast, the equilibrium inter-electrode distance for the T-type configuration is 2.34 nm for all three junctions, which is about 0.23 nm longer than that for the S-type configuration. The energy minima for the O-type configuration of the M2 and M3 junctions occur at an inter-electrode distance of 2.06 nm, which is very close to the value 2.11 nm for the S-type configuration of the M2 and M3 junctions. Notably, for both M2 and M3 junctions, the O-type configuration is energetically more favorable than the S-type configuration. In addition, for the M2 junction, during the compressing process, the T-type configuration tends to transition back to its original S-type or O-type configuration from the stretching process. Differently, for M3 junction, the T-type configuration would prefer to transition to the O-type configuration during the compressing process regardless of its original configuration from the stretching process.

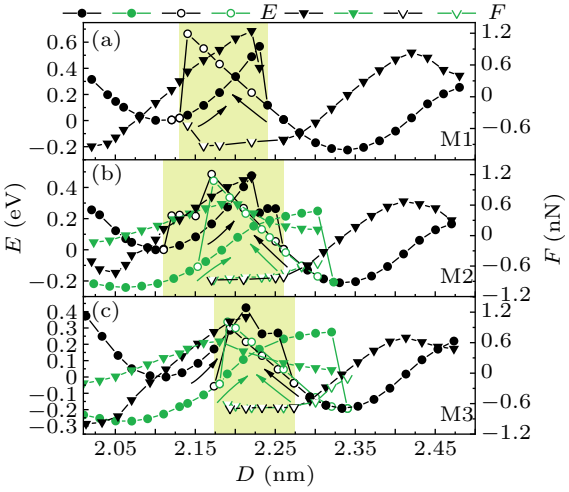


Fig. 3. The variations in energy (solid and hollow circles) and force (solid and hollow triangles) of (a) M1, (b) M2, and (c) M3 molecular junctions in the adiabatic stretching and compressing processes. The shaded areas in pale yellow–green indicate the inter-electrode distances for which irreversible contact configuration evolutions occur during the stretching and compressing processes. The solid circles and triangles indicate the stretching process, and the hollow circles and triangles indicate the compress process. The data in black are related to the S-type and/or T-type configurations while those data in green are related to the O-type configuration.

For all three junctions, the maximum stretching force required for the S-type configuration to transition to the T-type configuration is approximately 1.2 nN. However, only about 0.7 nN–0.8 nN is needed to finally break the junctions by pulling the upper pyridyl away from the upper tip electrode. This is consistent with the experiment observations that the maximum stretching force for the high-conductance state at a shorter inter-electrode distance ($\sim$ 1.48 nN) is evidently larger than the force needed to completely break the DPMJs at the low-conductance state ($\sim$ 0.85 nN).[40] For the M2 and M3 junctions, the force required to break the O–Au binding is about 0.6 nN–0.7 nN, which is also notably smaller than the 1.2 nN required to pull the upper pyridyl away from the second Au atomic layer.

3.3. Electronic transport properties and HLCS behavior of investigated DPMJs

To understand the HLCS behavior of investigated DPMJs, we then examine the conductance evolution of the M1, M2, and M3 molecular junctions during the stretching and compressing processes, which are shown in Fig. 4. It is evident that all the investigated DPMJs with the S-type configuration exhibit high conductance. However, as the configuration evolves from the S-type configuration to the T-type configuration, the junctions transition from a high-conductance state to a low-conductance state. It is noted that M2 and M3 junctions with O-type configuration also manifest a low-conductance state, of which the conductance values are similar to those in the T-type configuration. This suggests that configuration conversions of the DPMJs between T-type and O-type configurations do not result in a noticeable HLCS behavior. On the contrary, the HLCS behavior of M1 and M2 junctions arises from the configuration conversion between the S-type and T-type configurations during the stretching and compressing of the inter-electrode distance. The insets of Figs. 4(a) and 4(b) further demonstrate that when the inter-electrode distance is cyclically elongated and compressed between 2.10 nm and 2.33 nm/2.34 nm, the conductance of M1 and M2 junctions switches between high and low values, as observed in the experiment.[46] As shown in Fig. 4(c), for the M3 junction, though the S-type configuration would contribute to a high-conductance state, it cannot be maintained during the stretching and compressing processes. As discussed above, the S-type configuration transitions to the O-type configuration during the subsequent compressing process. As a result, the high-conductance state and the HLCS behavior are difficult to observe experimentally for the M3 junction. It should be mentioned that for the M1 and M2 junctions, there is overlap in the conductance evolution between the stretching and compressing processes. This implies that a much smaller modulation of the inter-electrode distance than the overlap regions in the M1 and M2 single-molecule junctions would significantly reduce the probability of observing the HLCS behavior. Conversely, a much larger modulation could lead to the breakdown of the single-molecule junctions. The overlap regions range from 2.12 nm to 2.24 nm for the M1 junction and from 2.10 nm to 2.23 nm for the M2 junction. These overlap values are con-

sistent with the experimental observation that a 0.2-nm modulation in the inter-electrode distance is optimal for achieving clean, reproducible HLCS behavior.

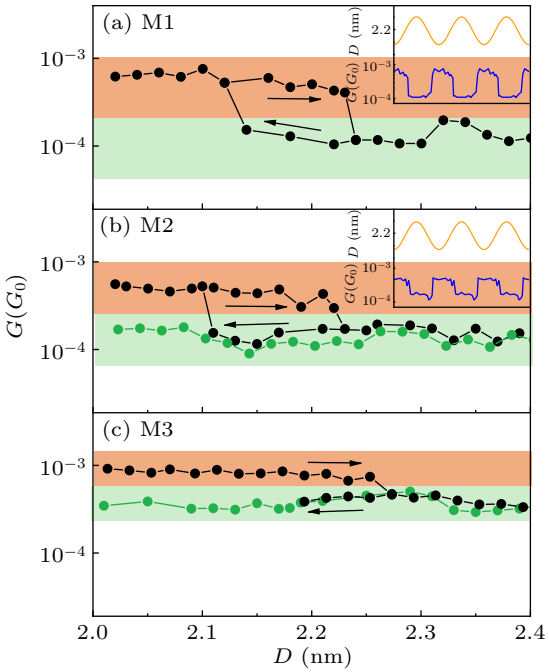


Fig. 4. Conductance evolution of (a) M1, (b) M2, and (c) M3 junctions during adiabatic stretching and compressing processes. The insets of panels (a) and (b) show that the conductance of M1 and M2 junctions can be cyclically switched between high and low values by repeatedly elongating and compressing the inter-electrode distance.

The influence of different contact configurations on the electronic transport properties of the investigated junctions can be further understood by examine the spatial distributions of the potential field, which is a crucial factor affecting the electronic transmission coefficient. Figure 5 shows the spatial distributions of the potential field for the M2 junction with S-type and T-type configurations and for the M3 junction with O-type and T-type configurations. It is found that, for the M2 junction with the S-type configuration shown in Fig. 5(a), there is an obvious potential well channel (potential wells are denoted by white lines) and a wide lower potential area (lower potential areas are denoted by black lines) between the M2 molecule and upper tip electrode, which favors electron transport between the molecule and tip electrode. In contrast, for the M2 and M3 junctions with the T-type configuration shown in Figs. 5(b) and 5(d), no obvious potential well channel is observed. Instead, only a narrow lower potential area exists between the molecules and the upper tip electrode, which hinders electron transport. For M3 junction with the O-type configuration shown in Fig. 5(c), the stronger electronegativity of the oxygen atom causes the potential well channel between the oxygen atom and the apical Au atom to be discrete, and the lower potential area is much narrower than that with S-type configuration. As a result, the M3 junction as well as M2 junction with the O-type configuration show a low conductance.

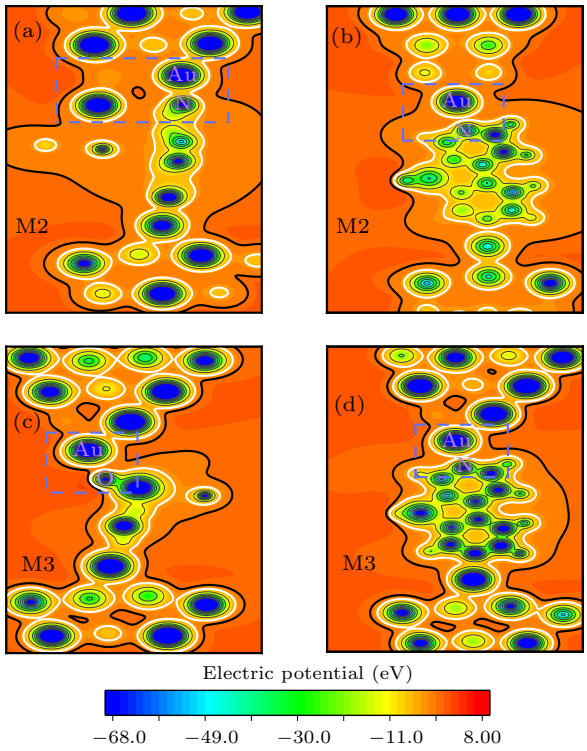


Fig. 5. Spatial distributions of potential field (in units of eV) for the M2 junction with (a) S-type configuration and (b) T-type configuration. Spatial distributions of potential field for the M3 junction with (c) O-type configuration and (d) T-type configuration. The dashed blue rectangles denote the contact areas between the upper pyridyl and the tip electrode. The white lines are the contour line of −4.6 eV while the black lines are the contour line of −0.6 eV.

4. Conclusion

The adiabatic configuration evolution of 4,4′-dipyridyl based single-molecule junctions as well as the effect of side groups are studied using the first-principles calculations. The numerical results show that, at small inter-electrode distances, the pyridyl tends to vertically adsorb onto the second Au atomic layer of the tip electrode (S-type configuration), which leads to stronger molecule–electrode coupling and a high-conductance state the junctions. As the electrode gap is further elongated, the pyridyl shifts to the apical Au atom of the tip electrode (T-type configuration), resulting in a low-conductance state of the junctions due to weaker molecule–electrode coupling and additional scattering, diffraction and reflection from the apical Au atom. For the junctions with phenyl-phosphoryl and cyclohexyl-phosphoryl side groups containing an oxygen atom, the oxygen atom preferentially adsorbs on the apical Au atom of the tip electrode at small inter-electrode distances (O-type configuration). For the M2 junction, both O-type and S-type configurations can exist. However, for the M3 junction, when it is compressed, the T-type configuration transitions only to the O-type configuration regardless of its original configuration formed during the stretching process. This results in the disappearance of the HLCS behavior for the M3 junction. Our results provide a theoretical understanding of the side-group effects on electronic transport

properties of single-molecule junctions and offer an alternative explanation for the experimental observations.

Acknowledgement

Project supported by the National Natural Science Foundation of China (Grant Nos. 12474286, 22173052, and 12204281).

References

[1] Lörtscher E 2013 *Nat. Nanotechnol.* **8** 381
[2] Haedler A T, Kreger K, Issac A, Wittmann B, Kivala M, Hammer N, Köhler J, Schmidt H and Hildner R 2015 *Nature* **523** 196
[3] Reed M A, Zhou C, Muller C J, Burgin T P and Tour J M 1997 *Science* **278** 252
[4] Xu B Q, Li X L, Xiao X Y, Sakaguchi H and Tao N J 2005 *Nano Lett.* **5** 1491
[5] Xiang D, Jeong H, Kim D, Lee T, Cheng Y J, Wang Q L and Mayer D 2013 *Nano Lett.* **13** 2809
[6] Vezzoli A, Grace I, Brooke C, Wang K, Lambert C J, Xu B Q, Nichols R J and Higgins S J 2015 *Nanoscale* **7** 18949
[7] Xiang D, Wang X L, Jia C C, Lee T and Guo X F 2016 *Chem. Rev.* **116** 4318
[8] Jia C C, Migliore A, Xin N, Huang S Y, Wang J Y, Yang Q, Wang S P, Chen H L, Wang D M, Feng B Y, Liu Z R, Zhang G Y, Qu D H, Tian H, Ratner M A, Xu H Q, Nitzan A and Guo X F 2016 *Science* **352** 1443
[9] Chen D H, Yang Z, Fu X Y, Qin S A, Yan Y, Wang C K, Li Z L and Qiu S 2024 *Chin. Phys. B* **33** 047201
[10] Li H X, Garner M H, Su T A, Jensen A, Inkpen M S, Steigerwald M L, Venkataraman L, Solomon G C and Nuckolls C 2017 *J. Am. Chem. Soc.* **139** 10212
[11] Liu R, Bi J J, Xie Z, Yin K, Wang D, Zhang G P, Xiang D, Wang C K and Li Z L 2018 *Phys. Rev. Appl.* **9** 054023
[12] Yan Y, Sun F, Yang Z, Kong C Y, Ge Y L, Chen D H, Qiu S and Li Z L 2024 *Acta Phys. Sin.* **73** 088502 (in Chinese)
[13] Tan M, Sun F, Zhao X, Zhao Z, Zhang S, Xu X, Adijiang A, Zhang W, Wang H, Wang C, Li Z, Scheer E and Xiang D 2024 *J. Am. Chem. Soc.* **146** 6856
[14] Li H, Garner M H, Shangguan Z, Chen Y, Zheng Q, Su T A, Neupane M, Liu T, Steigerwald M L, Ng F, Nuckolls C, Xiao S X, Solomon G C and Venkataraman L 2018 *J. Am. Chem. Soc.* **140** 15080
[15] Xie X M, Li P H, Xu Y X, Zhou L, Yan Y, Xie L H, Jia C C and Guo X F 2022 *ACS Nano* **16** 3476
[16] Liu R, Han Y M, Sun F, Khatri G, Kwon J, Nickle C, Wang L J, Wang C K, Thompson D, Li Z L, Nijhuis C A and Barco E D 2022 *Adv. Mater.* **34** 2202135
[17] Metzger R M 2009 *Synth. Met.* **159** 2277
[18] Guo C L, Wang K, Zerah-Harush E, Hamill J, Wang B, Dubi Y and Xu B Q 2016 *Nat. Chem.* **8** 484
[19] Sun F, Liu R, Liu L, Yan Y, Wang S S, Yang Z, Suo Y Q, Wang C K and Li Z L 2022 *Physica E* **140** 115186
[20] Fu H Y, Sun F, Liu R, Suo Y Q, Bi J J, Wang C K and Li Z L 2019 *Phys. Lett. A* **383** 867
[21] Niu L L, Fu H Y, Suo Y Q, Liu R, Sun F, Wang S S, Zhang G P, Wang C K and Li Z L 2021 *Physica E* **128** 114542
[22] Li H X, Su T A, Zhang V, Steigerwald M L, Nuckolls C and Venkataraman L 2015 *J. Am. Chem. Soc.* **137** 5028
[23] Li H X, Garner M H, Shangguan Z C, Zheng Q W, Su T A, Neupane M, Li P P, Velian A, Steigerwald M L, Xiao S X, Nuckolls C, Solomon G C and Venkataraman L 2016 *Chem. Sci.* **7** 5657
[24] Zhang G P, Mu Y Q, Zhao J M, Huang H, Hu G C, Li Z L and Wang C K 2019 *Physica E* **109** 1
[25] Zheng C F, Mu Y Q, Li Z L and Zhang G P 2024 *Chin. J. Chem. Phys.* **37** 644
[26] Zhang C Y, Kong Y Q, Xiang J J, Chen S K, Kornyshev A A, Ulstrup J, Gao X K, Zhang G P, Li Y Q and Li J H 2025 *Chem. Sci.* **16** 1353
[27] Yi X H, Liu R, Bi J J, Jiao Y, Wang C K and Li Z L 2016 *Chin. Phys. B* **25** 128503
[28] Li Z L, Bi J J, Liu R, Yi X H, Fu H Y, Sun F, Wei M Z and Wang C K 2017 *Chin. Phys. B* **26** 098508
[29] Zhou M, Lu Y H, Cai Y Q, Zhang C and Feng Y P 2011 *Nanotechnology* **22** 385502
[30] Yuan L, Wang L J, Garrigues A R, Jiang L, Annadata H V, Antonana M A, Barco E and Nijhuis C A 2018 *Nat. Nanotechnol.* **13** 322
[31] Wang Z Q, Tang F, Dong M M, Wang M L, Hu G C, Leng J C, Wang C K and Zhang G P 2020 *Chin. Phys. B* **29** 067202
[32] Bai J, Li X H, Zhu Z Y, Zheng Y and Hong W J 2021 *Adv. Mater.* **33** 2005883
[33] Zhang G P, Sun Y Z, Shi N P, Yu C J, Kong Y Q, Huang H and Wang Z Q 2023 *Chin. J. Chem. Phys.* **36** 707
[34] Xu B Q and Tao N J 2003 *Science* **301** 1221
[35] Xu B Q, Xiao X Y and Tao N J 2003 *J. Am. Chem. Soc.* **125** 16164
[36] Quek S Y, Kamenetska M, Steigerwald M L, Choi H J, Louie S G, Hybertsen M S, Neaton J B and Venkataraman L 2009 *Nat. Nanotechnol.* **4** 230
[37] Suo Y Q, Liu R, Sun F, Niu L L, Wang S S, Liu L and Li Z L 2020 *Acta Phys. Sin.* **69** 208502 (in Chinese)
[38] Kamenetska M, Quek S Y, Whalley A C, Steigerwald M L, Choi H J, Louie S G, Nuckolls C, Hybertsen M S, Neaton J B and Venkataraman L 2010 *J. Am. Chem. Soc.* **132** 6817
[39] Hong W J, Manrique D Z, Moreno-García P, Gulcur M, Mishchenko A, Lambert C J, Bryce M R and Wandlowski T 2012 *J. Am. Chem. Soc.* **134** 2292
[40] Aradhya S V, Frei M, Hybertsen M S and Venkataraman L 2012 *Nat. Mater.* **11** 872
[41] Kim T, Darancet P, Widawsky J R, Kotiuga M, Quek S Y, Neaton J B and Venkataraman L 2014 *Nano Lett.* **14** 794
[42] Mezei G, Balogh Z, Magyarkuti A and Halbritter A 2020 *J. Phys. Chem. Lett.* **11** 8053
[43] Magyarkuti A, Balogh Z, Mezei G and Halbritter A 2021 *J. Phys. Chem. Lett.* **12** 1759
[44] Sun F, Liu L, Zheng C F, Li Y C, Yan Y, Fu X X, Wang C K, Liu R, Xu B Q and Li Z L 2023 *Nanoscale* **15** 12586
[45] Liu L, Sun F, Li Y C, Yan Y, Liu B X, Yang Z, Qiu S and Li Z L 2023 *Acta Phys. Sin.* **72** 048504 (in Chinese)
[46] Ismael A K, Wang K, Vezzoli A, Al-Khaykanee M K, Gallagher H E, Grace I M, Lambert C J, Xu B Q, Nichols R J and Higgins S J 2017 *Angew. Chem. Int. Ed.* **56** 15378
[47] Li Z L, Zhang G P and Wang C K 2011 *J. Phys. Chem. C* **115** 15586
[48] Zhao Z K, Liu R, Mayer D, Coppola M, Sun L, Kim Y, Wang C K, Ni L F, Chen X, Wang M N, Li Z L, Lee T and Xiang D 2018 *Small* **14** 1703815
[49] Zhao X Y, Yan Y, Tan M, Zhang S R, Xu X N, Zhao Z B, Wang M N, Zhang X B, Adijiang A, Li Z L, Scheer E and Xiang D 2024 *SmartMat* **5** e1280
[50] Frisch M J, Trucks G W, Schlegel H B, *et al.* 2016 Gaussian 16 Rev. A. 03 (Wallingford, CT)
[51] Liu R, Wang C K and Li Z L 2016 *Sci. Rep.* **6** 21946
[52] Shankar R 1994 *Principles of Quantum Mechanics*, 2nd Edn. (New York: Plenum Press) pp. 164–175